

<https://helda.helsinki.fi>

ALMA Survey of Orion Planck Galactic Cold Clumps (ALMASOP) : Density Structure of Centrally Concentrated Prestellar Cores from Multiscale Observations

Sahu, Dipen

2023-03-01

Sahu , D , Liu , S-Y , Johnstone , D , Liu , T , Evans II , N J , Hirano , N , Tatematsu , K , Di
Francesco , J , Lee , C-F , Kim , K-T , Dutta , S , Hsu , S-Y , Li , S , Luo , Q-Y , Sanhueza , P
, Shang , H , Traficante , A , Juvela , M , Lee , C W , Eden , D J , Goldsmith , P F , Bronfman
, L , Kwon , W , Lee , J-E , Kuan , Y-J & Ristorcelli , I 2023 , ' ALMA Survey of Orion Planck
Galactic Cold Clumps (ALMASOP) : Density Structure of Centrally Concentrated Prestellar
Cores from Multiscale Observations ' , Astrophysical Journal , vol. 945 , no. 2 , 156 . <https://doi.org/10.3847/1538-43>

<http://hdl.handle.net/10138/357200>

<https://doi.org/10.3847/1538-4357/acbc26>

cc_by

publishedVersion

Downloaded from Helda, University of Helsinki institutional repository.

This is an electronic reprint of the original article.

This reprint may differ from the original in pagination and typographic detail.

Please cite the original version.



ALMA Survey of Orion Planck Galactic Cold Clumps (ALMASOP): Density Structure of Centrally Concentrated Prestellar Cores from Multiscale Observations

Dipen Sahu^{1,2}, Sheng-Yuan Liu², Doug Johnstone^{3,4}, Tie Liu⁵, Neal J. Evans II⁶, Naomi Hirano², Ken'ichi Tatematsu⁷, James Di Francesco^{3,4}, Chin-Fei Lee², Kee-Tae Kim^{8,9}, Somnath Dutta², Shih-Ying Hsu^{2,10}, Shanghuo Li¹¹, Qiu-Yi Luo⁵, Patricio Sanhueza^{12,13}, Hsien Shang², Alessio Traficante¹⁴, Mika Juvela¹⁵, Chang Won Lee^{8,9}, David J. Eden¹⁶, Paul F. Goldsmith¹⁷, Leonardo Bronfman¹⁸, Woojin Kwon^{19,20}, Jeong-Eun Lee²¹, Yi-Jehng Kuan^{2,22}, and Isabelle Ristorcelli²³

¹ Physical Research laboratory, Navrangpura, Ahmedabad, Gujarat 380009, India; dsahu@prl.res.in

² Academia Sinica Institute of Astronomy and Astrophysics, 11F of AS/NTU Astronomy-Mathematics Building, No. 1, Sec. 4, Roosevelt Rd., Taipei 10617, Taiwan, R.O.C.

³ NRC Herzberg Astronomy and Astrophysics, 5071 West Saanich Rd., Victoria, BC V9E 2E7, Canada

⁴ Department of Physics and Astronomy, University of Victoria, Victoria, BC V8P 5C2, Canada

⁵ Shanghai Astronomical Observatory, Chinese Academy of Sciences, 80 Nandan Road, Shanghai 200030, People's Republic of China

⁶ Department of Astronomy, The University of Texas at Austin, 2515 Speedway, Stop C1400, Austin, TX 78712-1205, USA

⁷ Nobeyama Radio Observatory, National Astronomical Observatory of Japan, National Institutes of Natural Sciences, 462-2 Nobeyama, Minamimaki, Minamisaku, Nagano 384-1305, Japan

⁸ Korea Astronomy and Space Science Institute, 776 Daedeokdae-ro, Yuseong-gu, Daejeon 34055, Republic of Korea

⁹ University of Science and Technology, Korea (UST), 217 Gajeong-ro, Yuseong-gu, Daejeon 34113, Republic of Korea

¹⁰ National Taiwan University (NTU), Taiwan, R.O.C.

¹¹ Max Planck Institute for Astronomy, Königstuhl 17, D-69117 Heidelberg, Germany

¹² National Astronomical Observatory of Japan, National Institutes of Natural Sciences, 2-21-1 Osawa, Mitaka, Tokyo 181-8588, Japan

¹³ Department of Astronomical Science, SOKENDAI (The Graduate University for Advanced Studies), 2-21-1 Osawa, Mitaka, Tokyo 181-8588, Japan

¹⁴ IAPS-INAF, via Fosso del Cavaliere 100, I-00133, Rome, Italy

¹⁵ Department of Physics, P.O.Box 64, FI-00014, University of Helsinki, Finland

¹⁶ Armagh Observatory and Planetarium, College Hill, Armagh, BT61 9DB, UK

¹⁷ Jet Propulsion Laboratory, California Institute of Technology, 4800 Oak Grove Drive, Pasadena, CA 91109, USA

¹⁸ Departamento de Astronomía Universidad de Chile, Camino el Observatorio 1515, Las Condes, Santiago, Chile

¹⁹ Department of Earth Science Education, Seoul National University, 1 Gwanak-ro, Gwanak-gu, Seoul 08826, Republic of Korea

²⁰ SNU Astronomy Research Center, Seoul National University, 1 Gwanak-ro, Gwanak-gu, Seoul 08826, Republic of Korea

²¹ Department of Physics and Astronomy, Seoul National University, 1 Gwanak-ro, Gwanak-gu, Seoul 08826, Republic of Korea

²² Department of Earth Sciences, National Taiwan Normal University, Taipei, Taiwan (R.O.C.)

²³ Université de Toulouse, UPS-OMP, IRAP, F-31028 Toulouse cedex 4, France

Received 2022 December 5; revised 2023 February 7; accepted 2023 February 9; published 2023 March 16

Abstract

Starless cores represent the initial stage of evolution toward (proto)star formation, and a subset of them, known as prestellar cores, with high density ($\sim 10^6 \text{ cm}^{-3}$ or higher) and being centrally concentrated are expected to be embryos of (proto)stars. Determining the density profile of prestellar cores therefore provides an important opportunity to gauge the initial conditions of star formation. In this work, we perform rigorous modeling to estimate the density profiles of three nearly spherical prestellar cores among a sample of five highly dense cores detected by our recent observations. We employed multiscale observational data of the (sub)millimeter dust continuum emission, including those obtained by SCUBA-2 on the James Clerk Maxwell Telescope with a resolution of ~ 5600 au and by multiple Atacama Large Millimeter/submillimeter Array observations with a resolution as high as ~ 480 au. We are able to consistently reproduce the observed multiscale dust continuum images of the cores with a simple prescribed density profile, which bears an inner region of flat density and an r^{-2} profile toward the outer region. By utilizing the peak density and the size of the inner flat region as a proxy for the dynamical stage of the cores, we find that the three modeled cores are most likely unstable and prone to collapse. The sizes of the inner flat regions, as compact as ~ 500 au, signify them as being the highly evolved prestellar cores rarely found to date.


Unified Astronomy Thesaurus concepts: [Molecular clouds \(1072\)](#); [Collapsing clouds \(267\)](#); [Infrared dark clouds \(787\)](#); [Star formation \(1569\)](#); [Astronomical methods \(1043\)](#); [Astronomy data modeling \(1859\)](#)

1. Introduction

Starless cores are dense fragments in molecular clouds but without the association of (proto)stars. A subset of starless cores that are gravitationally unstable, dubbed prestellar cores (PSCs), will be prone to collapse and eventually form (proto)

stars (Crapsi et al. 2005; di Francesco et al. 2007). These PSCs, therefore at the first stage of star formation, offer the best opportunity to gauge the initial conditions of star formation. Characterizing their structures, such as density and temperature profiles, is essential for testing theoretical models and for understanding the physical processes of star formations (Andre et al. 2000).

Observationally, the density profile of starless/prestellar cores can be estimated from the dust continuum emission, the dust extinction, and/or emission from molecular lines. The

 Original content from this work may be used under the terms of the [Creative Commons Attribution 4.0 licence](#). Any further distribution of this work must maintain attribution to the author(s) and the title of the work, journal citation and DOI.

latter method can be less accurate, as tracer species get depleted onto the dust grains at the low temperatures and high densities within the PSCs. Using near-IR extinction observations, Alves et al. (2001) estimated the density profile of the dark core B68. They found that the density profile closely fit with the theoretical description of the Bonner–Ebert (BE) sphere (Ebert 1955; Bonnar 1956), which represents a class of externally pressure-bound self-gravitating isothermal cores. In particular, B68 is found to be a “critical” BE sphere configuration, suggesting that the core is on the verge of instability.

Studies by Ward-Thompson et al. (1994), Andre et al. (1996), Ward-Thompson et al. (1999), and Bacmann et al. (2000) used millimeter dust continuum observations to estimate PSC density profiles, finding that the density profile of starless/prestellar cores can be fitted with power laws that are steeper in the outer region and shallower in the inner region. Based on similar observations, Tafalla et al. (2002) suggested that the density profile of starless cores can be better fit by the following equation:

$$\rho(r) = \frac{\rho_c}{1 + (r/a)^\alpha}, \quad (1)$$

where r is the radial distance, a is the radial size of the inner flat region, and α is the power-law index. Now, with $\alpha=2$ in Equation (1), the underlying profiles resemble the BE sphere model. Dapp & Basu (2009) used this type of equation with a fixed power law, $\alpha=2$, and emphasized that the generic features of the BE sphere are not unique to equilibrium conditions but also appear in gravitationally collapsing objects. Additionally, the authors argued that the flat region size can be used as a proxy for core evolution. Estimation of the flat region size of PSCs is therefore important (see also Keto & Caselli 2008, 2010).

When using optically thin dust emission for characterizing the density structures of the PSCs and for inferring their evolution, multiscale observations are indispensable. Single-dish telescopes can image the full core scale but cannot provide sufficient angular resolution to capture the central zone. Interferometric observations typically resolve out the large-scale structures of the starless core but constrain the size of the inner flat region. Indeed, for L1544, which is one of the most studied cores having both single-dish and interferometric observations (e.g., Ohashi et al. 1999; Caselli et al. 2019), the derived column density profile based on single-dish observations varies as r^{-1} , with a flatter region within $r \sim 3000$ au (Caselli et al. 2002). Detailed fitting using an unstable BE sphere model required that the flat extent of L1544 is $\gtrsim 1500$ au (Keto & Caselli 2010; Keto et al. 2014).

To date, only a few PSCs have been studied in detail (e.g., Crapsi et al. 2004; Schmalzl et al. 2014) owing to the limited number of candidate cores. The lack of known PSCs is most likely due to a combination of source structure and limited sensitivity (see introduction section of Sahu et al. 2021, for more details). In particular, the structure of the innermost region within the PSCs had been least studied (Caselli et al. 2019). Recently, Sahu et al. (2021) detected five PSCs in Orion, which are centrally dense and have peak densities that are quite high (10^6 – 10^7 cm^{-3}) relative to other known PSCs, such as L1544 ($\sim 10^6$ cm^{-3}), and “starless” cores L1498 and L1517B (Tafalla et al. 2004).

The primary motive of the present work is to estimate the density profile from small ($\lesssim 1000$ au) to large ($\sim 10,000$ au) scales toward the three comparatively spherical PSCs among the above five, namely G209.94-19.52N, G212.10-19 15N1, and G205.46-14.46M3 (hereafter G209N, G212N1, and G205M3, respectively). We estimate the peak density and the size of flat regions of these PSCs consistently through multiscale observations, and we use these measurements as proxies for the cores’ dynamical state.

The paper is organized as follows: In Section 2 we describe the observations. In Sections 3 we introduce the physical model and the methodology. Results of the modeling are described in Section 4. The limitations and implications of the model results are discussed in Section 5. Finally, in Section 6 we summarize our findings. Other relevant information is provided in the appendices.

2. Observations

2.1. Single-dish Observations

As a part of the James Clerk Maxwell Telescope (JCMT) SCOPE survey (proposal code: M16AL003), 58 Planck Galactic Cold Clumps (PGCCs) were observed across the Orion A, Orion B, and λ Orionis molecular clouds. The Submillimetre Common-User Bolometer Array 2 (SCUBA-2) instrument (Holland et al. 2013) at the JCMT was used to map the 850 μm dust continuum emission at an angular resolution $\sim 14''$; details of the full data set are described by Yi et al. (2018). Figure 1 uses gray contours to plot the JCMT 850 μm dust continuum emission toward the three Orion cores G209N, G212N1, and G205M3.

2.2. Interferometric Observations: ALMA

ALMASOP (project ID: 2018.1.00302.S) Atacama Large Millimeter/submillimeter Array (ALMA) observations were carried out in Cycle 6 toward 72 fields selected from the above JCMT SCOPE survey. The observations were executed in the 1.3 mm band using three different array configurations: 12 m C43-5 (TM1), 12 m C43-2 (TM2), and 7 m ACA, resulting in angular resolutions ranging from $0''.34$ to $5''.5$. The correlator was configured into four spectral windows with 1.875 GHz bandwidth each. We adopted a coarse velocity resolution of 1.129 MHz, equivalent to 1.5 km s^{-1} , to facilitate efficient continuum observations and maximize spectral line coverage. The remaining details of the observational parameters are presented in Dutta et al. (2020).

The visibility data were calibrated with the Common Astronomy Software Applications (CASA; McMullin et al. 2007) 5.4 pipeline script as delivered by the observatory. The visibility data for all configurations and executions toward each of the 72 fields were then separated into continuum and spectral lines and imaged jointly. The 1.3 mm continuum images of each field were generated through CASA’s *tclean* task with the “automask” on, the hogbom deconvolver, and a robust weighting of 0.5 for data acquired with different arrays. The ACA-only 1.3 mm continuum images toward the three cores, G209N, G212N1, and G205M3, are shown in Figure 1 in blue, with red contours at a $5''.5$ resolution. In addition, all three cores were also detected by the 12 m array in configuration TM2 in combination with ACA at $1''.2$ resolution. Figure 2 shows a magnified view of the cores using the high-resolution TM2 observations in color and ACA observations overplotted

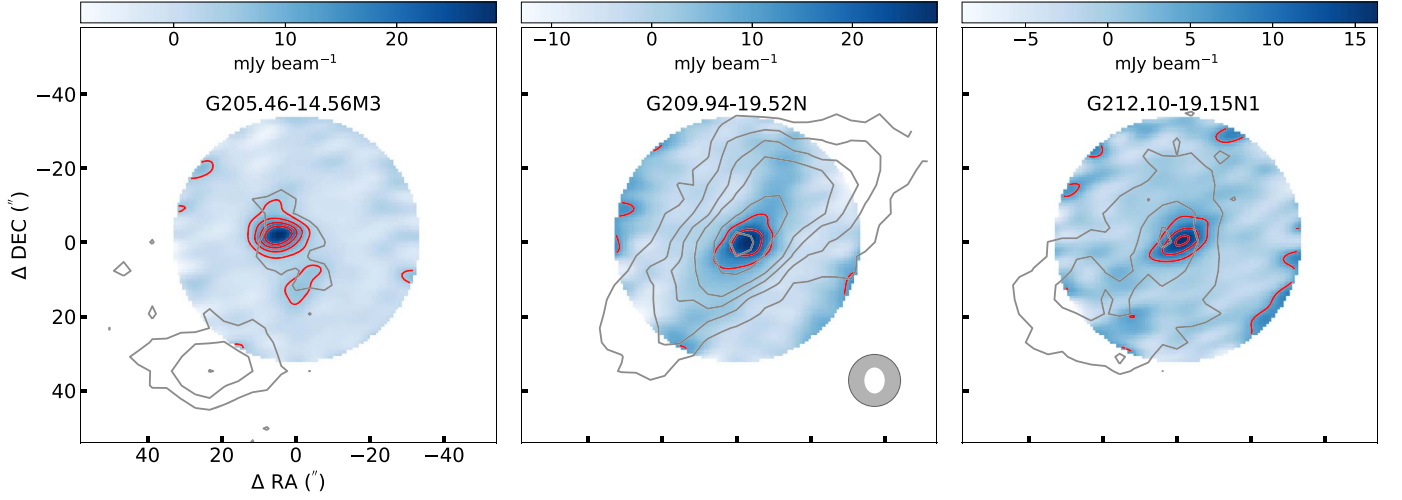


Figure 1. The 1.3 mm dust continuum emission of the three PSCs (in blue) as observed with ACA-ALMA; red contours correspond to 5σ , 10σ , and 15σ , where σ (rms) are 1.0, 2.0, and 1.0 mJy beam^{-1} , respectively. The gray contours correspond to 0.85 mm SCUBA-2 emission with similar contour levels where $\sigma(\text{rms}) = 44.5$, 13.9, and 16.4 mJy beam^{-1} , respectively. The beams of SCUBA-2 and ACA are shown in the middle panel.

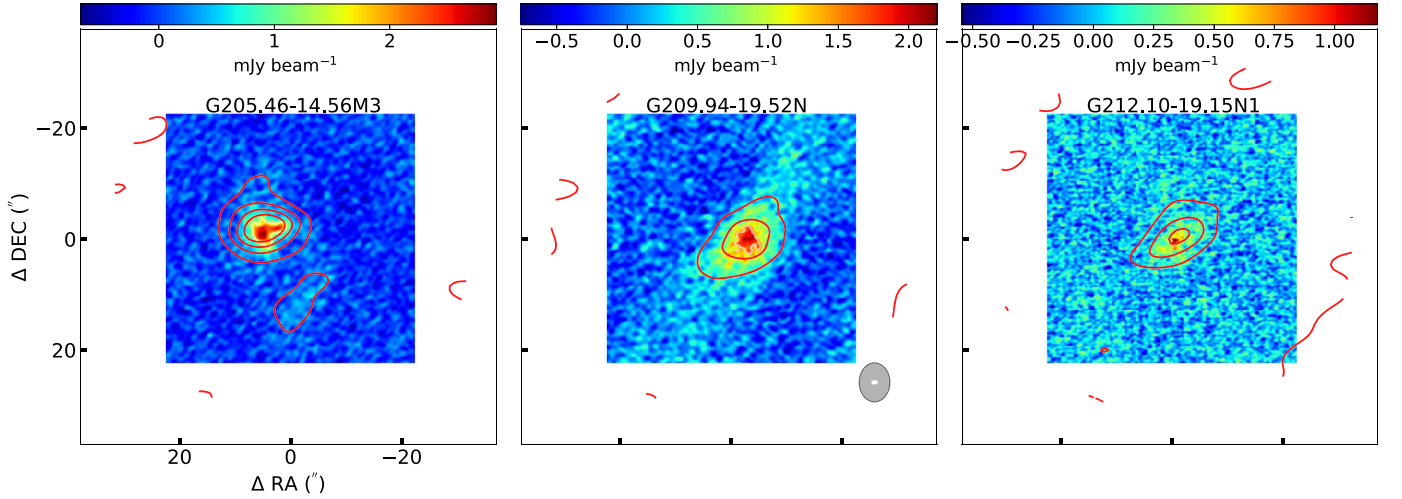


Figure 2. The 1.3 mm dust continuum emission of the three PSCs—color scale from ACA+TM2 combined data (resolution $\sim 1''.2$). The red contours correspond to ACA observations similar to those shown in Figure 1. The beam sizes of the ACA and TM2+ACA configuration are represented in the middle panel.

in contours. As noted in Sahu et al. (2021), these PSCs are resolved out by the 12 m TM1 array at a resolution $\sim 0''.3$.

3. Physical Model and Methodology

For inferring the density profile of the observed PSCs, we adopt the parametric function proposed in Dapp & Basu (2009),

$$\rho(r) = \begin{cases} \frac{\rho_c a^2}{r^2 + a^2} & \text{for } r \leq R, \\ 0 & \text{for } r > R. \end{cases} \quad (2)$$

Here ρ_c is the peak volume density (n_c , corresponding number density), a is the size of the inner flat region, and R is the outer radius of the core.

An analytical column density profile can be integrated from Equation (2) as shown by Dapp & Basu (2009):

$$\Sigma(x) = \frac{\Sigma_c}{\sqrt{1 + (x/a)^2}} \times \left[\arctan \left(\frac{c^2 - (x/a)^2}{\sqrt{1 + (x/a)^2}} \right) / \arctan(c) \right] + d, \quad (3)$$

where Σ_c is the peak column density and $c = R/a$. The flat radius is given by $a = k \frac{C_s}{\sqrt{(G\rho)}}$, where C_s is the sound speed, G is the gravitational constant, and k is a free variable proportionality constant. The peak column density is related to the peak density via the relation $\Sigma_c = 2a n_c \arctan(c)$. In the equation above, we include an additional term d to represent the gas column density due to the extended ambient cloud

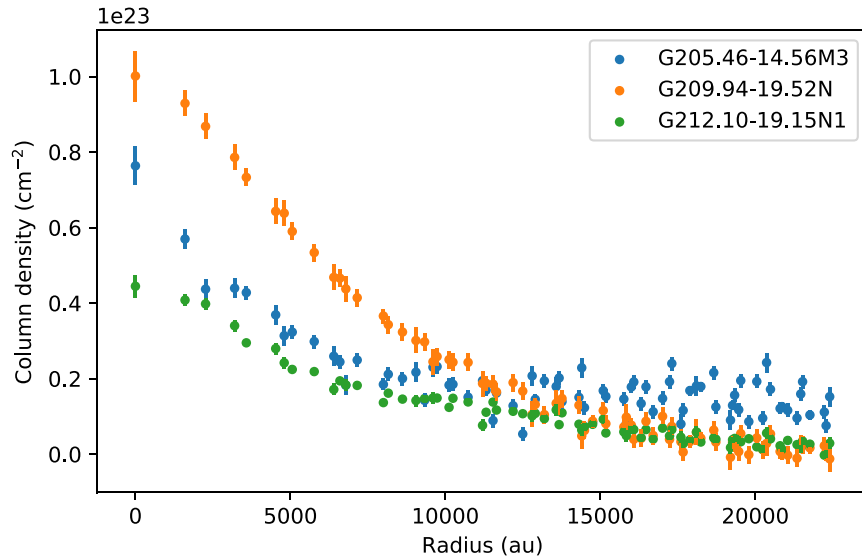


Figure 3. Azimuthally averaged column density profile of the three PSCs as obtained from SCUBA-2 dust continuum emission. The error bars in the profile are the statistical errors obtained by σ/\sqrt{n} , where σ is rms noise obtained from the emission map and “ n ” is the number of pixels corresponding to the radial distance bin used to obtain the radially averaged flux values.

surrounding the PSC. It is to be noted that the underlying assumption of Equation (2) is the isothermal condition. Subsequently, we assume a constant temperature and opacity through the cores. The above assumption works well with the scope of this study, and we discuss further in Section 5.1 the possible implications.

To extract the underlying density profile of each observed core, we first estimate the column density profile from the annular-averaged dust continuum intensity profile at $850\ \mu\text{m}$ observed with the JCMT by assuming that the emission is optically thin with a dust absorption coefficient (κ) $\sim 2.23\ \text{cm}^2\ \text{g}^{-1}$ and that the dust temperature is 10 K throughout (Figure 3). These profiles are then compared against the analytic column density profile (Equation (3)) after the latter gets convolved with a Gaussian profile representing the JCMT beam FWHM $\sim 14''$. By fitting the radial profiles, we determine the outer boundary R of each PSC and the constant offset d due to the cloud. We also determine a rough estimate of the peak density ρ_c and the flat radius a guiding the multiscale imaging synthesis and fitting.

With the outer edge of each PSC R determined, we generate a set of 2000 synthetic model 1.3 mm continuum images by varying a with 40 linearly spaced values between 10 and 4000 au and n_c with 50 logarithmic-spaced points between 10^5 and $10^9\ \text{cm}^{-3}$, as input models for the radiative transfer code SPARX.²⁴ A dust temperature of 10 K throughout the cores and a dust absorption coefficient of $\sim 0.9\ \text{cm}^2\ \text{g}^{-1}$ from Ossenkopf & Henning (1994) corresponding to thick icy dust at $10^6\ \text{cm}^{-3}$ are adopted. The radiative transfer code, with fixed temperature, ensures that any nonnegligible optical depth near the core center is properly taken into account during the calculation.

The telescope-related interferometric effects are further considered through imaging simulations using CASA. We incorporate the same telescope configuration as in the original ALMA observations, process the above synthetic model images using the “simobserve” task, and produce visibility

data sets for each of the 2000 synthetic models. We use the “tclean/simanalyse” task, as we did for the real observed images, to further produce mock continuum emission maps, which can then be directly compared with the observed images.

We estimate the best-fit parameters by comparing the radial intensity profiles between the observed and simulated images using χ^2 fitting. For each core, separate χ^2 fittings were conducted for the images observed at multiple scales with the JCMT and the ALMA ACA and TM2 configurations. The multiscale approach is necessary, as the core emission at large physical, and hence angular, scales is best detected by single-dish telescopes and not the interferometric observations. Contrariwise, the inner radial features, smaller than 2800 au in size, are poorly constrained by the JCMT SCUBA-2 observations, given the $14''$ beam size of SCUBA-2 at the distance of the Orion cores (~ 400 pc).

We present the $\Delta\chi^2$ plots corresponding to 1σ value (see Figures C1, C2, C3) for each set of observations in order to estimate consistent model parameters for the observed images at all scales. The best parameters for minimizing χ^2 over the individual maps and for the global optimization are given in Table 1. We find that the flat radius a of the cores is small, 300–1400 au, and describe below the results for each individual core in detail.

4. Results

The major aim of our multiscale imaging modeling is to estimate the overall size of the PSC, R , the size of the inner flat region at the center of the core, a , and the associated peak density, ρ_c , using the assumed physical model (Equation (2)). As the cores are found with $R/a > 10$, their masses are also approximated as $M \sim 4\pi\rho_c a^2 R$, within an uncertainty of $<15\%$ (Dapp & Basu 2009). The size of the inner flat region acts as a proxy of PSC evolution, and based on our estimation, the PSCs presented here possibly are the most evolved and compact (i.e., have the smallest flat region) compared to the PSC samples found in the literature. Below, we discuss the three PSCs individually.

²⁴ <https://sparx.tiara.sinica.edu.tw/>

Table 1
Fitting Results for the Three Cores

| Core Parameters | | | |
|----------------------|---------------------------|--------------|--------------|
| Method | n_c (cm ⁻³) | (a in au) | (au) |
| G205M3 | | | |
| Analytical model fit | 1.35×10^6 (0.91) | 924 (410) | 10720 (1983) |
| SCUBA cont fit* | 3.4×10^7 | 214.6 | ... |
| ACA cont fit | 1.1×10^7 | 521 | ... |
| TM2+ACA cont fit | 1.3×10^7 | 419 | ... |
| Global fit | 1.1×10^7 | 521 | ... |
| Plotted values | 1.1×10^7 | 419, 521 | ... |
| G209N | | | |
| Analytical model fit | 6.08×10^5 (0.76) | 2891 (254) | 17178 (770) |
| SCUBA cont fit | 1.4×10^6 | 2158.4 | ... |
| ACA cont fit | 2.4×10^6 | 1749 | ... |
| TM2+ACA cont fit | 3.6×10^6 | 1135 | ... |
| Global fit | 2.9×10^6 | 1340 | ... |
| Plotted values | 2.9×10^6 | 1340 | ... |
| G212N1 | | | |
| Analytical model fit | 8.6×10^5 (7.18) | 1009 (548) | 7357 (214) |
| SCUBA cont fit | 2.9×10^6 | 726 | ... |
| ACA cont fit* | 1.3×10^6 | 1544 | ... |
| TM2+ACA) cont fit | 9.1×10^6 | 214 | ... |
| Global fit | 5.2×10^6 | 316 | ... |
| Plotted values | 5.2×10^6 | 316, 521 | ... |

Note. The core radii obtained using the analytical fitting are presented in row 1, with its error bar shown in parentheses. The best-fit values obtained from grid search for different telescope configurations are presented in rows 2–5; note that the uncertainties are not noted in the table and visually presented in Appendix C. The global fit represents the best-fit parameter values considering multiscale observations. For G205M3, Figure 4 shows the profile plots with the “global fit” parameter values for ACA and 12 m TM2 observations, while for the case of SCUBA-2, “ a ” \sim 419 au is used. For G209N, Figure 5 shows a similar plot with the global parameter values obtained. In the case of G212N1, Figure 6 is a plot using global parameter values for the TM2 configuration, while for the ACA and SCUBA-2 case $n_c \sim 5.2 \times 10^6$ cm⁻³ and “ a ” \sim 521 au is used.

4.1. G205M3

Among the sample PSCs, G205M3 is the only core that shows substructure at the 1000 au scale (see Figure 2 and Sahu et al. 2021, for details). The SCUBA-2 image (see Figure 1) shows that the core is clearly separated from another nearby core to the SE.

Within the core, however, a fainter second peak, roughly 20'' SW from center, can be seen in both the SCUBA-2 and ACA maps. Despite the substructure, the approximation of a spherically symmetric structure for the radial profile derivation is reasonable given the weakness and distance of the secondary feature.

Figure 4 shows that the radial profile of G205M3 flattens out beyond a radial distance of about 12,000 au. The constant though noisy profile beyond 12,000 au may be due to the ambient molecular cloud environment. From fitting the SCUBA-2 column density profile, we find an outer radius of \sim 11,000 au. Combining all the estimations from different observing configurations, the best global fit values are $n_c = 1.1 \times 10^7$ cm⁻³ and $a \sim$ 500 au. The global parameter values can be estimated from the plot (see Figure C1)—the

values corresponding to the common region of $\Delta\chi^2$ contours. The estimated PSC mass is $2.2 M_\odot$, implying that roughly 30% of the emission was resolved out by the ACA observations (mass $1.7 M_\odot$, for a temperature of 10 K and the same dust opacity; see Sahu et al. 2021).

We note that for G205M3 the derived average number density within the flat region (500 au) is $\sim 7 \times 10^6$ cm⁻³, about two times higher than that of $\sim 3.0 \times 10^6$ cm⁻³ toward L1544 found by Keto & Caselli (2010).

4.2. G209N

The G209N core is comparatively larger and more elongated than G205M3, with no substructure present at the single-dish scale (\sim 10,000 au). In the higher-resolution interferometric observations, unlike G205M3, G209N shows a dense central peak with a nearly circular shape.

Through an analysis similar to that for G205M3, the outer radius, R , of G209N is found to be $42''.5$ or \sim 17,000 au at a distance of 400 pc (see Figure 5). The best-fit parameters, using our multiscale observations, are constrained to be $n_c \sim 2.9 \times 10^6$ cm⁻³ and $a \sim$ 1300 au. These values are listed in Table 1 (see also Figure C2). For G209N, the average number density within the flat region $\sim 2 \times 10^6$ cm⁻³ may be slightly smaller than or similar to that of L1544 (Keto & Caselli 2010; Caselli et al. 2019). The mass inferred for G209N is $10.5 M_\odot$. Given its large outer radius, a significant fraction of emission was resolved out by the ACA, which detected a mass of only $2.7 M_\odot$ (Sahu et al. 2021).

4.3. G212N1

Toward G212N1, a secondary peak can be seen $\sim 25''$ to the SE in the SCUBA-2 map (Figure 1). Assuming that this nearby source, beyond 8500 au, is a separate entity, we focus on the densest substructure detected by ALMA (ACA and TM2 configurations) toward the field center (see Figure 2). The core radius, R , is found to be \sim 7400 au from the column density profile fitting, and the profile plots related to each of the observing configurations are presented in Figure 6.

From the $\Delta\chi^2$ plots (see Figure C3), there is no obvious common parameter region corresponding to the SCUBA-2, ACA, and TM2 observations, though the contours are quite close and have partial overlap. Thus, the best-fit results for each different observational setup are noted in Table 1. The peak density $\sim 5.2 \times 10^6$ cm⁻³ and the size of the flat region $a \sim$ 320 au corresponding to the global fit do not simultaneously fit well the observed intensity profiles from different observations. The small flat inner region is determined from the 12 m TM2 observation and the corresponding profile. Fixing the best-fit peak density $\sim 5.2 \times 10^6$ cm⁻³, we find a somewhat larger flat region $a \sim$ 520 au for the ACA and SCUBA-2 observations. Within a reasonable uncertainty, a peak density $\sim 5.2 \times 10^6$ cm⁻³ and $a \sim$ 320–520 au closely describe the central zone across the multiscale observations.

The core radius, R , of G212N1 is significantly smaller, \sim 7000 au, than for the other two Orion PSCs, and the dust continuum emission is more likely fully recovered by the ACA observations—the theoretically estimated core mass is $\sim 0.95 M_\odot$, close to the value of $1.0 M_\odot$ observed with the ACA (Sahu et al. 2021).

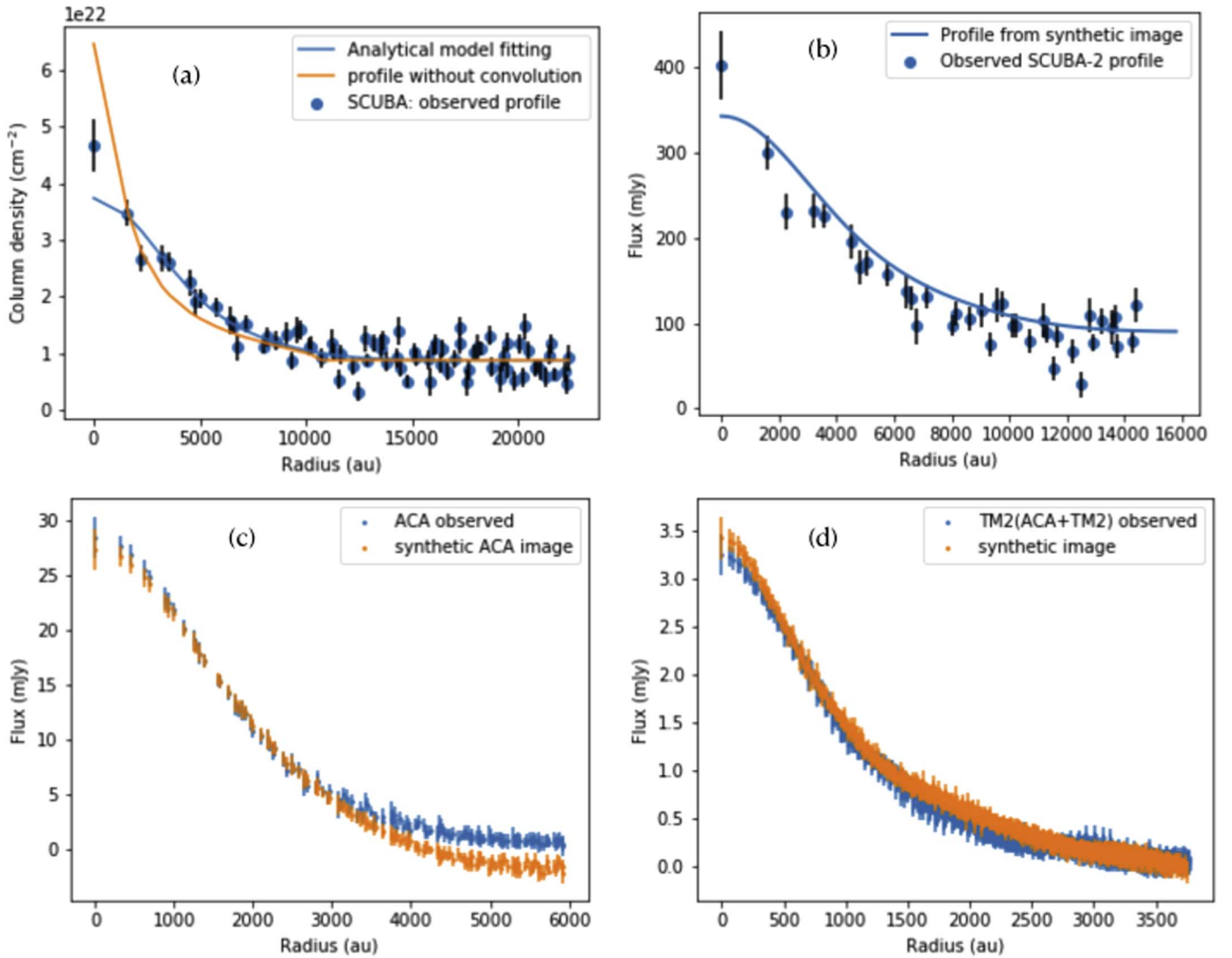


Figure 4. Radial column density profile fitting for the G205M3 core. (a) Simple analytical model fitting to determine the extent of core radius. (b) Profile fitting for SCUBA-2 observation with the profile from the model images corresponding to the end row values of Table 1. (c) Similar to panel (b), but for ACA observations. (d) Similar to panels (b) and (c), but for ACA+TM2 observations. The model parameters are noted in Table 1. A comparison between the modeled images and the observed maps is shown in Figure B1.

5. Discussion

5.1. Model Uncertainties from the Assumptions of Temperature and Dust Opacity

We have assumed a uniform temperature of 10 K for the cores both in the initial column density profile fitting for determining the outer radius and in the radiative transfer calculation for generating synthetic maps on the parameter grids. In the central region of the cores, however, the density is presumably higher and the temperature may be correspondingly lower as compared to the outer layers owing to efficient dust continuum cooling. Quantitatively, Crapsi et al. (2007), using high-resolution interferometric observations of NH_3 emission, found a drop in the gas temperature of ~ 5 K, and therefore well-coupled dust temperature, in the center of L1544.

To check the effect of a varying temperature profile on the inferred model parameters, we consider the temperature profile

given by Chacon-Tanarro et al. (2019):

$$T_{\text{out}} = T_{\text{out}} - \frac{T_{\text{out}} - T_{\text{in}}}{1 + \left(\frac{r}{a}\right)^{1.7}}, \quad (4)$$

estimated via a radiative transfer calculation for the PSC L1544. As the PSCs presented here are at least as centrally dense as L1544, we assume a similar temperature profile with $T_{\text{in}} = 6.9$ K and $T_{\text{out}} = 12$ K (Crapsi et al. 2007; Chacon-Tanarro et al. 2019). Using this temperature profile and the same parameter space as studied earlier, we find that, for G205M3, the best-fit peak density and flat radius (for 12 m TM2+ACA combined observations; compare with row 4 of Table 1) are $\approx 1.9 \times 10^7 \text{ cm}^{-3}$ and 320 au, respectively (Figure 7). Thus, qualitatively, the results imply that the inferred peak densities may be slightly higher ($\sim 50\%$) and the inner flat cores somewhat more compact ($\sim 25\%$). The

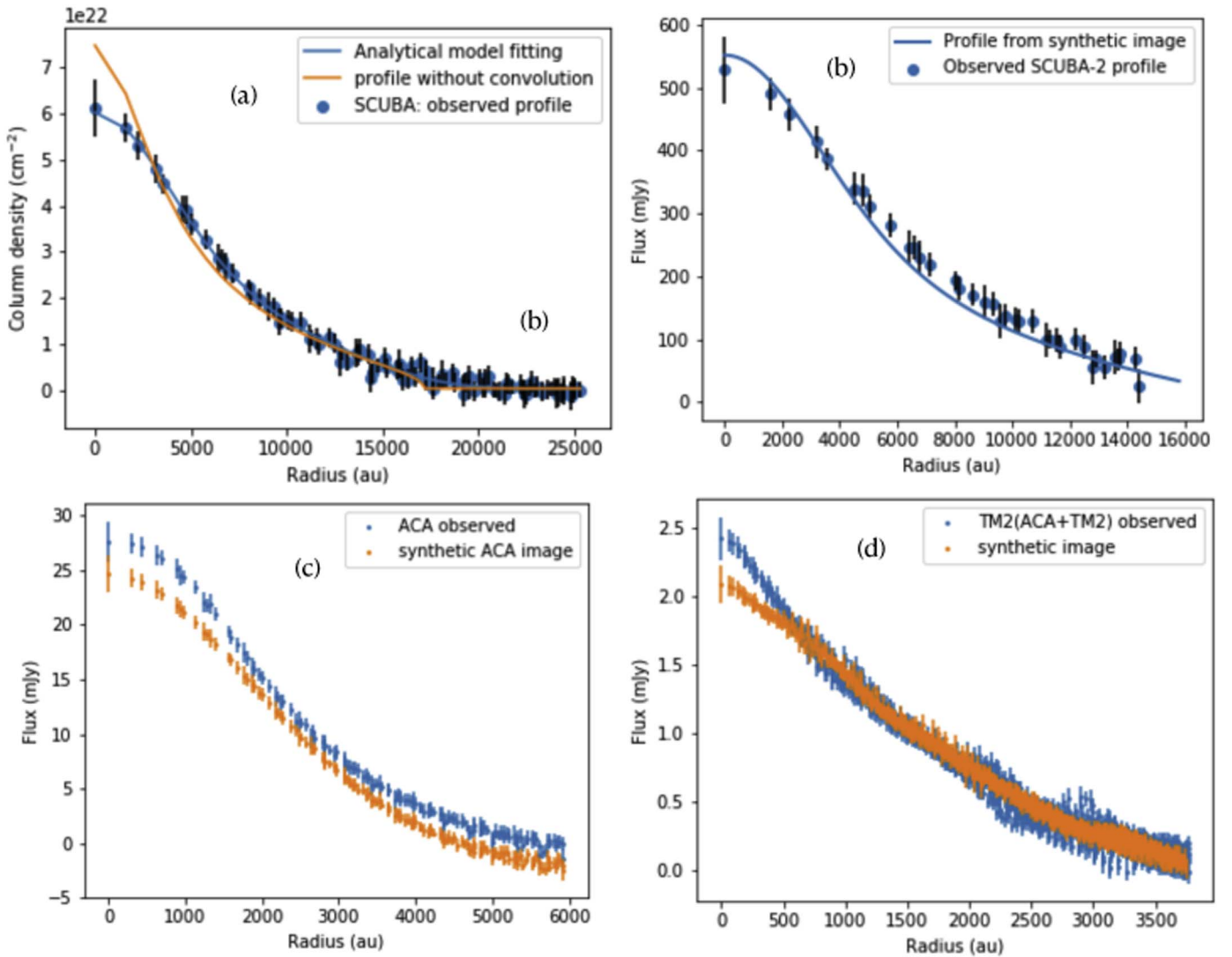


Figure 5. Similar to the fitting plots in Figure 4, but for the core G209N. The model parameters are noted in Table 1. A comparison between the modeled images and the observed maps is shown in Figure B2.

estimated values of peak density and flat radius will be similarly affected for other cores too.

Another assumption in the imaging modeling process, in addition to an isothermal temperature, is the choice of dust opacity used. For instance, Keto et al. (2014, and references therein) were successful in reproducing the molecular line and continuum observation of L1544 by considering temperature variations (Crapsi et al. 2007), but only if an increased/scaled dust opacity was included. Indeed, variations in dust opacity within molecular clouds have been deduced in recent years (see, e.g., Juvela et al. 2015; Sadavoy et al. 2016). The reasons for such opacity behavior are not clearly understood and highly uncertain. Recently, however, Chacon-Tanarro et al. (2019) studied in detail the effect of opacity on the density profile of the PSC L1544. By considering a radial opacity variation, they found that the corresponding best-fit density profile is comparatively flatter than that derived by Crapsi et al. (2007). Consequently, the peak density was also lower by a factor of 25%. Applying a radial temperature variation, we have already shown that the peak density becomes higher by about 50% and the source becomes more compact by around

25%. Thus, guided by the results of Chacon-Tanarro et al. (2019), we expect that our estimated parameters assuming isothermal and constant opacity conditions do not differ much from those if we consider the combined effect of temperature and opacity variations.

5.2. Choice of the Density Profile

Though their assumptions may differ, the theoretical models for star-forming cores such as the Larson core (Larson 1969), the inside-out collapse of a singular isothermal sphere (SIS; Shu 1977), and the quasi-equilibrium (QE) BE sphere (Bonnar 1956) all suggest that the gas densities in the outer region of a spherical core can be asymptotically described by the r^{-2} profile while the inner region exhibits a shallower radial dependence. Even nonspherical models that consider the effect of ambipolar diffusion and large-scale turbulence produce similar r^{-2} outer density profiles (Ciolek & Basu 2000).

Observational studies of starless/prestellar cores indeed seemed to find a central plateau in addition to power-law density profile in the outer region (e.g., Whitworth & Ward-

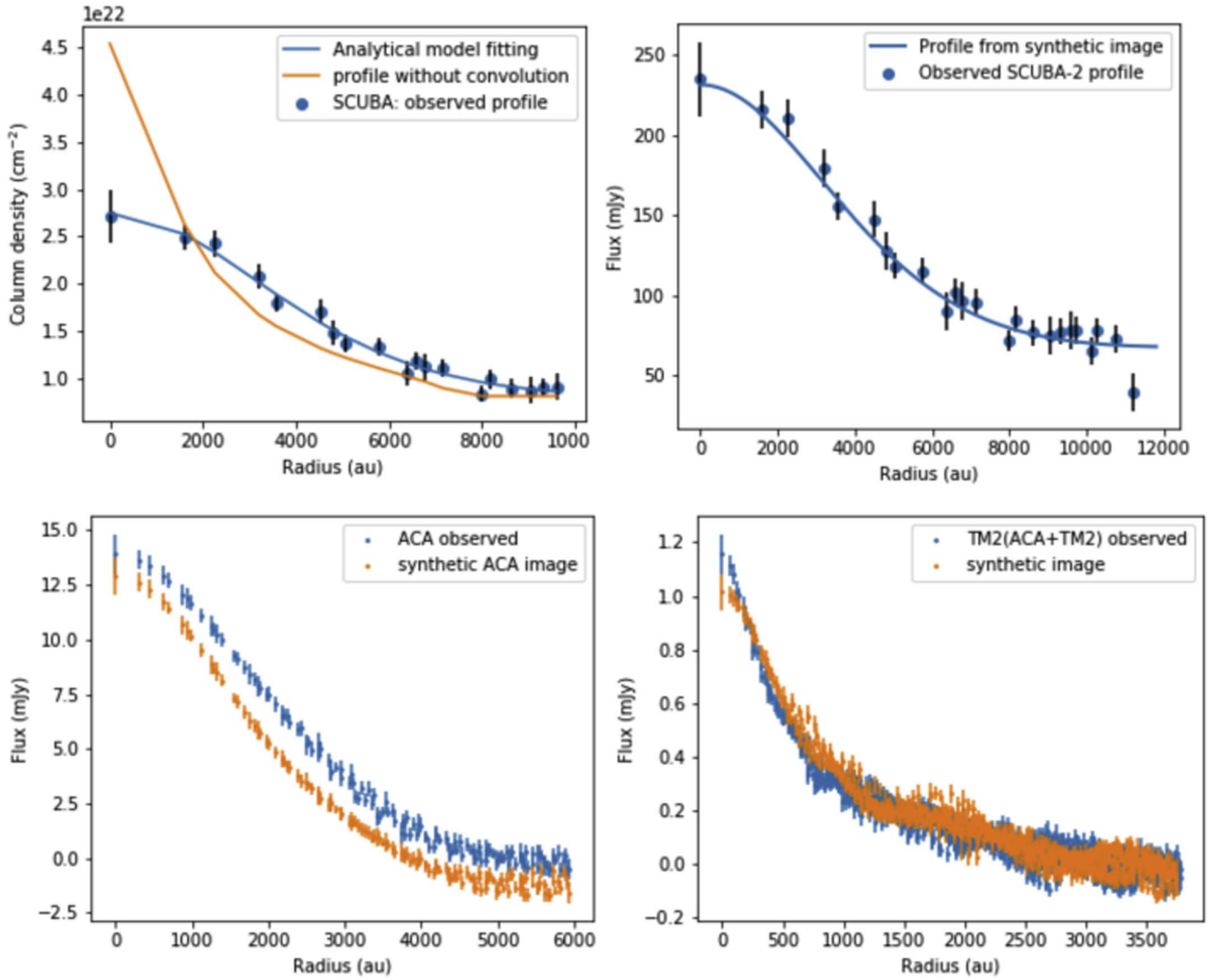


Figure 6. Similar to the fitting plots in Figure 4, but for the core G212N1. The model parameters are noted in Table 1. A comparison between the modeled images and the observed maps is shown in Figure B3.

Effect of temperature variation (G205M3)

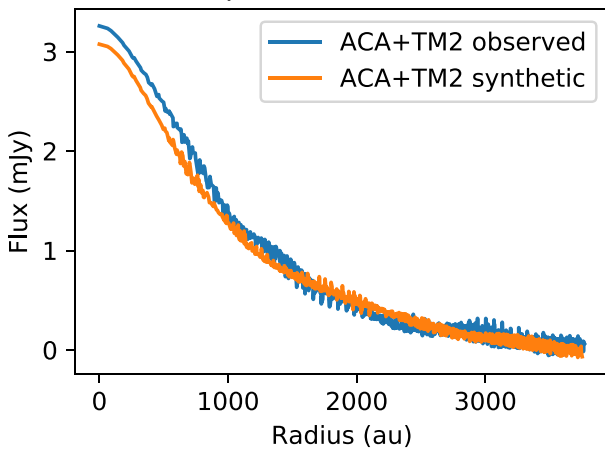


Figure 7. Effect of temperature variation for an example core G205M3. Here the model image’s n_c and “ a ” are $1.9 \times 10^7 \text{ cm}^{-3}$ and 316 au, respectively. These values can be compared with the values in Table 1, row 4.

Thompson 2001). For more general cases, Shirley et al. (2000), for example, found that the density profiles of low-mass cores lie in the range of $r^{-1.5}$ to $r^{-2.6}$ from a survey of 21 cores, including starless and protostellar objects. Hung et al. (2010) found two types of cores from their analysis of starless/prestellar cores—the “steep type,” which can be fit by a power-law slope of -2.5 , and the “shallow type,” which can be described by a power-law slope ~ -1.2 . Such more “exotic” shallow or steep power-law profiles may result from fitting the inner flat region and outer r^{-2} profile by a single power law, or the object is more protostellar in type instead of being starless (also see Kwon et al. 2009).

While protostellar cores are usually found to exhibit a power law of r^{-2} in their density profile (e.g., Shirley et al. 2000; Kwon et al. 2009), observational studies of starless/prestellar cores, in contrast, found that a central plateau in addition to a power law in the outer region indeed provides a better description for their density profile (e.g., Whitworth & Ward-Thompson 2001). For more general cases, Hung et al. (2010),

for example, found two types of cores from their analysis of starless/prestellar cores—the “steep type,” which can be fit by a power-law slope of -2.5 , and the “shallow type,” which can be described by a power-law slope ~ -1.2 . Their results suggested that the steeper-type starless cores are more evolved compared to the shallow type of cores. Gomez et al. (2021) indicated that the observed density profiles for starless cores with slopes steeper than -2.0 in fact could be mostly remedied by various observational uncertainties.

Motivated by the above, we adapted the proposition of Dapp & Basu (2009), an analytical density profile with an inner flat region and an outer r^{-2} profile as described in Equation (2). This model profile resembles that of the BE sphere but without the assumption of the core being in equilibrium. In addition, the temperature is treated as an input parameter for the model, as is done for our purposes. With the assumed r^{-2} profile, we were able to better determine the outer boundary of the cores, which helps to reduce the degeneracies between the central density, the flat region size, and the core size for a given peak column density.

5.3. Implications of the Flat Region Model Parameters

The model parameters of the flat region, including its central density and size, provide useful insights about the dynamical state of the core under consideration. In their work of modeling of starless cores, Keto & Caselli (2008) considered starless cores in two categories—those being thermally subcritical and those being thermally supercritical. The classification depends on whether their central density is below or above a few $\times 10^5 \text{ cm}^{-3}$, respectively. The central densities of the cores presented here are much higher than a few $\times 10^5 \text{ cm}^{-3}$, so the cores are arguably dynamically unstable and prone to dynamical collapse. The peak central density and the small flat region of G205M3, for example, may furthermore correspond to roughly a young dynamical age of a few $\times 10^5 \text{ yr}$ to 1 Myr in the model of Keto & Caselli (2010, see their Figure 1).

Indeed, Dapp & Basu (2009) also indicated that as the core evolves the core’s central density increases and the size of the flat region reduces. The inner flat region appears during the core evolution when the sound-crossing time is less than the freefall time and any density perturbations are rapidly smoothed up by the pressure waves within. Following this logic, the flat region size a value can be estimated as the product of sound speed, which depends on the gas temperature (which is assumed to be a constant here), and the freefall time, which inversely depends on the square root of the mean density of the enclosed mass and therefore drops as the central density increases. More explicitly, the flat region size can be expressed as $a = k \frac{c_s}{\sqrt{(G\rho_c)}}$, where k is the constant of proportionality and the latter part is the Jeans length. The analytical estimation from Dapp & Basu (2009) shows that for a BE sphere the core would be collapsing (i.e., supercritical) if $k \sim 0.6$ or higher. In the case of G205M3, with a flat region size of $\approx 500 \text{ au}$ and a peak density of $\approx 1.1 \times 10^7 \text{ cm}^{-3}$, the k value is ~ 0.7 . Similarly, for G209N, the k value is 0.9. If the temperature of the inner region is lower than 10 K, the k value would be even higher than those estimated values. Therefore, the cores G205M3 and G209N are likely to be collapsing to form protostar/protostars. For G212N1, the value of $k \sim 0.5$ is at the borderline for a collapsing core, and thus this core may be on the verge of collapse. Nevertheless, the set of PSCs represent the most compact (smaller flat region size) PSCs known to

date, and future spectral line observations toward the sample may provide direct evidence of collapsing signatures.

6. Conclusion

From our past ALMA observations we have found five highly dense and centrally compact PSCs, namely, G205.46-14.46M3, G208.68-19.20N2, G209.29-19.65S1, G209.94-19.52N, and G212.10-19 15N1 in Orion. Among the five PSCs, we found that three—G205.46-14.46M3, G209.94-19.52N, and G212.10-19 15N1 (in short G205M3, G209N1, and G212N1, respectively) are suitable to estimate the density profile with the assumption of underlying spherical shape. We further studied in detail the density profile of the three cores, considering the multiscale observations with beam sizes ranging from 5600 au (single-dish SCUBA-2) to 480 au (ALMA). To reproduce these cores’ density profile, we consider a physical model that includes a flat central region at the center and r^{-2} profile outside. The cores were assumed to be isothermal at 10 K. For two cores, G205M3 and G209N1, we found the density profile and dust continuum observation from the multiscale observations to be closely consistent with the assumed physical model. A slight deviation from the theoretical profile may be present for the third core G212N1, which has a prominent substructure at large scales ($\sim 10,000 \text{ au}$). The peak density, flat region size, and outer radius of the cores are found to be $\approx (1 \times 10^7 \text{ cm}^{-3}, 500 \text{ au}, 11,000 \text{ au})$, $(3 \times 10^6 \text{ cm}^{-3}, 1300 \text{ au}, 17,000 \text{ au})$, and $(5 \times 10^6 \text{ cm}^{-3}, 300 \text{ au}, 7000 \text{ au})$, respectively, for G205M3, G209N, and G212N1. Though we do not consider variations in core temperature and dust opacity, we found that these factors do not significantly affect the estimated peak density and flat region size. We used the estimated flat region size to gauge the dynamical state of the PSCs. The sizes of the flat regions imply that the cores are unstable and gravitationally collapsing or on the verge of collapse. Based on the estimated peak density and flat radius sizes, the cores in our current study belong to a rare sample of highly evolved PSCs known to date.

This paper makes use of the following ALMA data: ADS/JAO.ALMA#2018.1.00302.S. ALMA is a partnership of ESO (representing its member states), NSF (USA) and NINS (Japan), together with NRC (Canada), MOST and ASIAA (Taiwan), and KASI (Republic of Korea), in cooperation with the Republic of Chile. The Joint ALMA Observatory is operated by ESO, AUI/NRAO and NAOJ. D.S. acknowledges the support from SERB, Govt. of India, and PRL (A Unit of DoS) for continuing research and capacity building through the Ramanujan (Faculty) Fellow position. D.S. also acknowledges the support from Academia Sinica and TIARA (ASIAA) computing facilities. S.Y.L. acknowledges support from the National Science and Technology Council (NSTC) with grants 110-2112-M-001-056 and 111-2112-M-001-042. D.J. is supported by NRC Canada and by an NSERC Discovery Grant. T.L. is supported by the National Key R&D Program of China (No. 2022YFA1603100), National Natural Science Foundation of China (NSFC) through grants No. 12073061 and No.12122307, the international partnership program of Chinese Academy of Sciences through grant No. 1142 31KYSB20200009, Shanghai Pujiang Program 20PJ1415500, and the science research grants from the China Manned Space Project with no. CMS-CSST-2021-B06. N.H. acknowledges NSTC 110-2112-M-001-048 and NSTC 111-2112-M-001-060 grants. M.J. acknowledges support from the Academy of Finland

grant No. 348342. C.W.L. is supported by the Basic Science Research Program through the National Research Foundation of Korea (NRF) funded by the Ministry of Education, Science and Technology (NRF- 2019R1A2C1010851) and by the Korea Astronomy and Space Science Institute grant funded by the Korea government (MSIT; Project No. 2022-1-840-05). L.B. gratefully acknowledges support by the ANID BASAL projects ACE210002 and FB210003. W.K. was supported by the National Research Foundation of Korea (NRF) grant funded by the Korean government (MSIT) (NRF-2021R1F1A1061794). This research was carried out in part at the Jet Propulsion Laboratory, which is operated by the California Institute of Technology under a contract with the National Aeronautics and Space Administration

(80NM0018D0004). K.T. was supported by JSPS KAKENHI (Grant Number 20H05645).

Appendix A The Five Prestellar Cores

In the article, we discussed only the three cores among the five sample cores that were detected by Sahu et al. (2021); Figure A1 shows them all. Two of the five sample cores, G208N2 and G209S1, are very elongated and have asymmetric structures and are often treated as filaments (Ohashi et al. 2018). Hence, the radial profile estimation on the assumption of a spherically symmetric core is likely unsuitable in these cases and is excluded from the analysis.

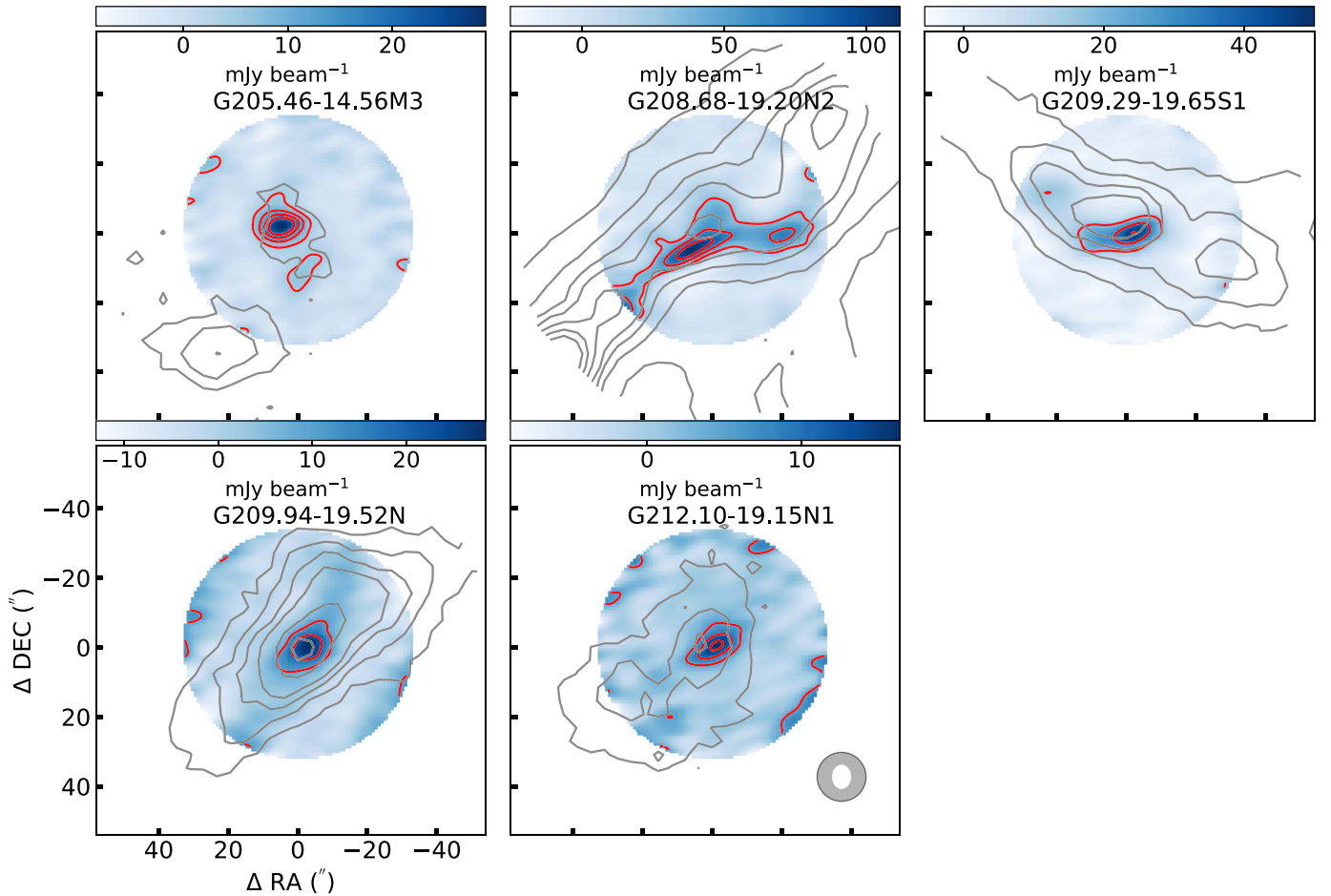


Figure A1. The 1.3 mm dust continuum emission of the five PSCs (in blue); red contours correspond to 5σ , 10σ , and 15σ , where $\sigma(\text{rms})$ is 1.0, 6.0, 3.3, 2.0, and 1.0 mJy beam^{-1} , respectively, for the cores G205M3, G208N2, G209N1, G209N, and G212N1. The gray contours correspond to 0.85 mm SCUBA-2 emission with similar contour levels where $\sigma(\text{rms}) = 44.5, 64.2, 31.3, 13.9,$ and $16.4 \text{ mJy beam}^{-1}$, respectively. The beams of SCUBA-2 and ACA are shown in the bottom right panel.

Appendix B Comparison of Emission Maps

In this appendix, Figures B1, B2, and B3 shows observed dust continuum versus synthetic model images of the three cores, G205M3, G209N, and G212N1, respectively. In the current analysis, the three cores are presented in this article.

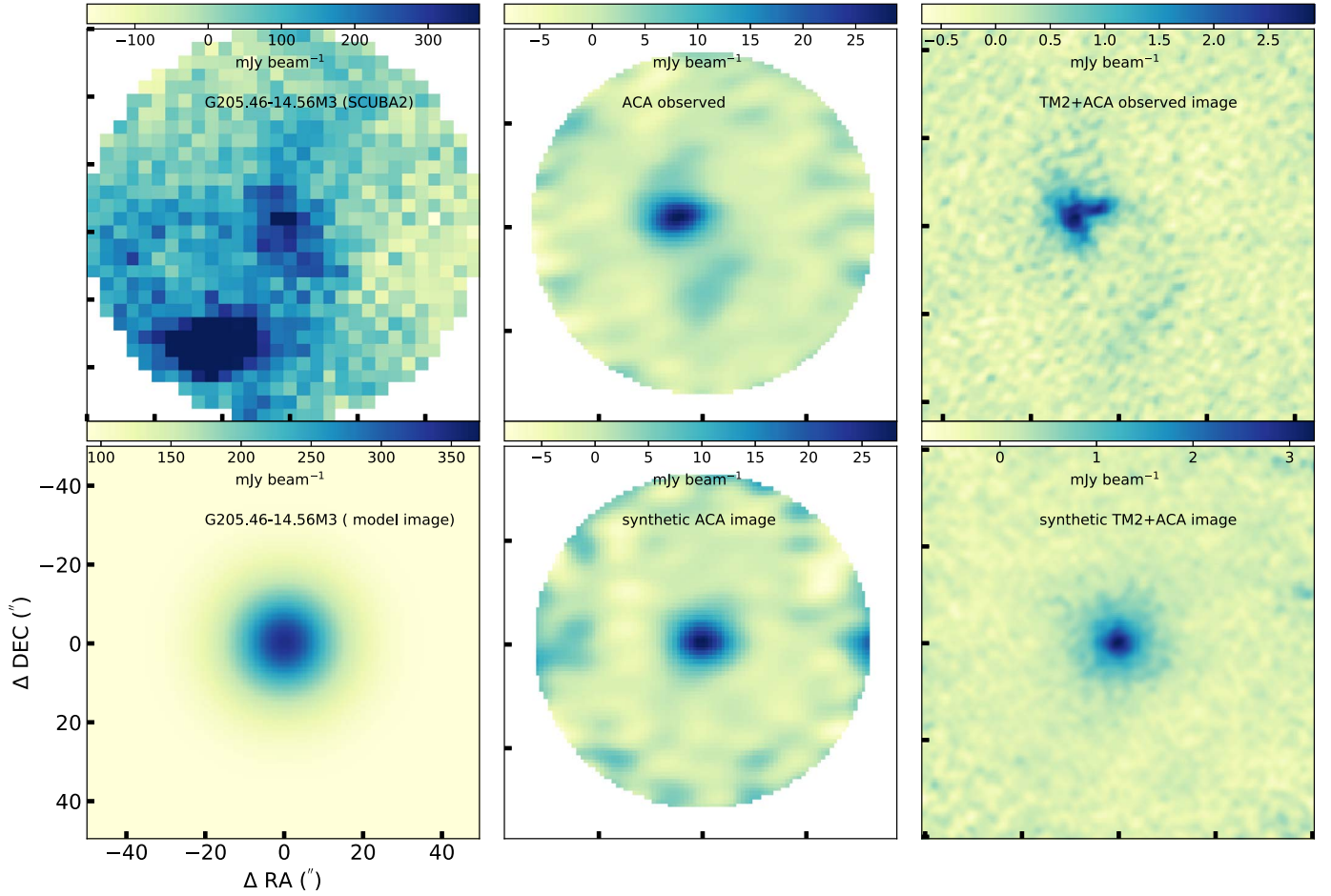


Figure B1. Top panels show the observed dust continuum from SCUBA-2, ACA, and TM2, respectively, toward the G205M3 core. The corresponding modeled synthetic images are shown in the bottom panels. The model images are based on the best-fit results that are presented in Figure 4 and Table 1.

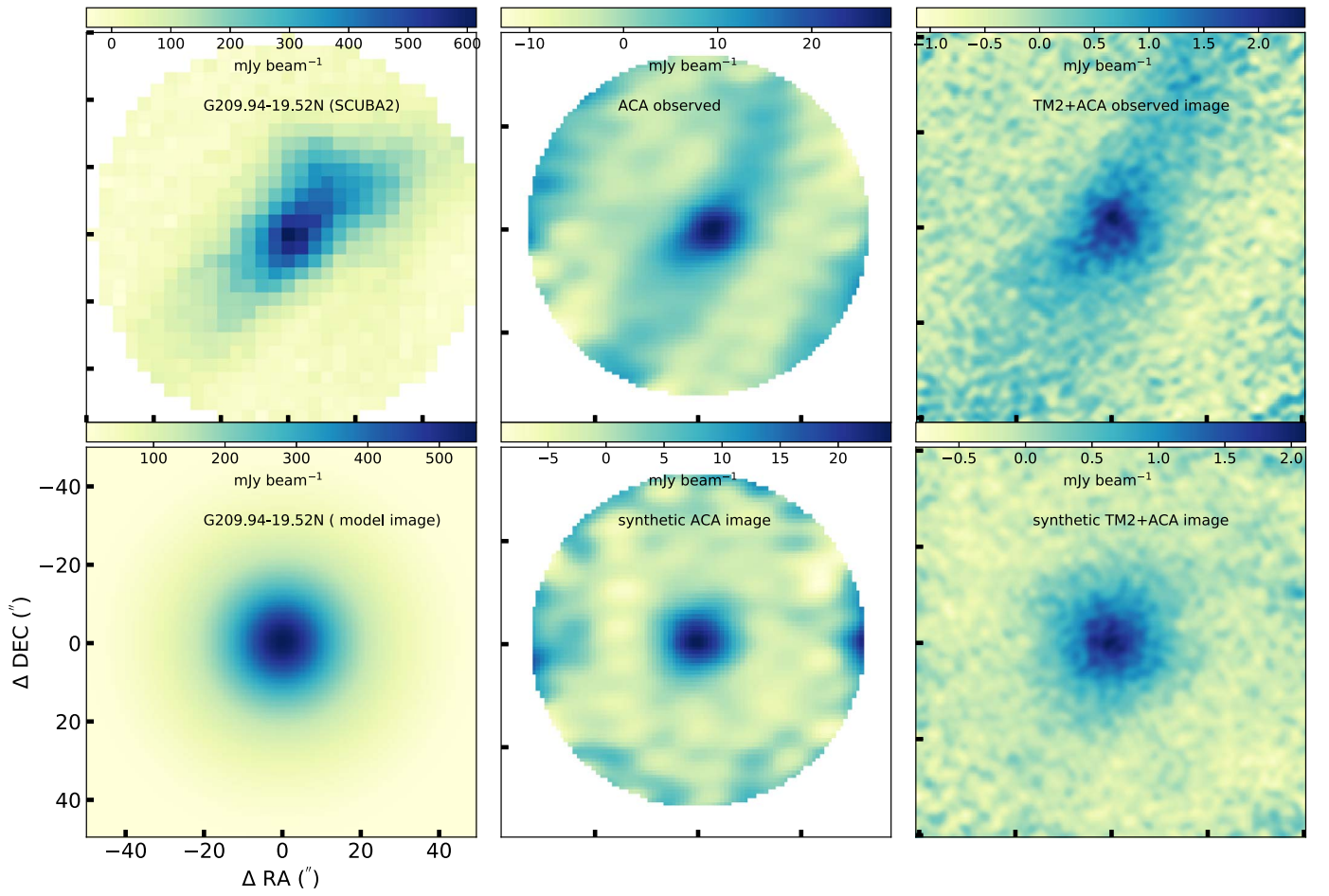


Figure B2. Top panels show the observed dust continuum from SCUBA-2, ACA, and TM2, respectively, toward the G209N core. The corresponding modeled synthetic images are shown in the bottom panels. The model images are based on the best-fit results that are presented in Figure 5 and Table 1.

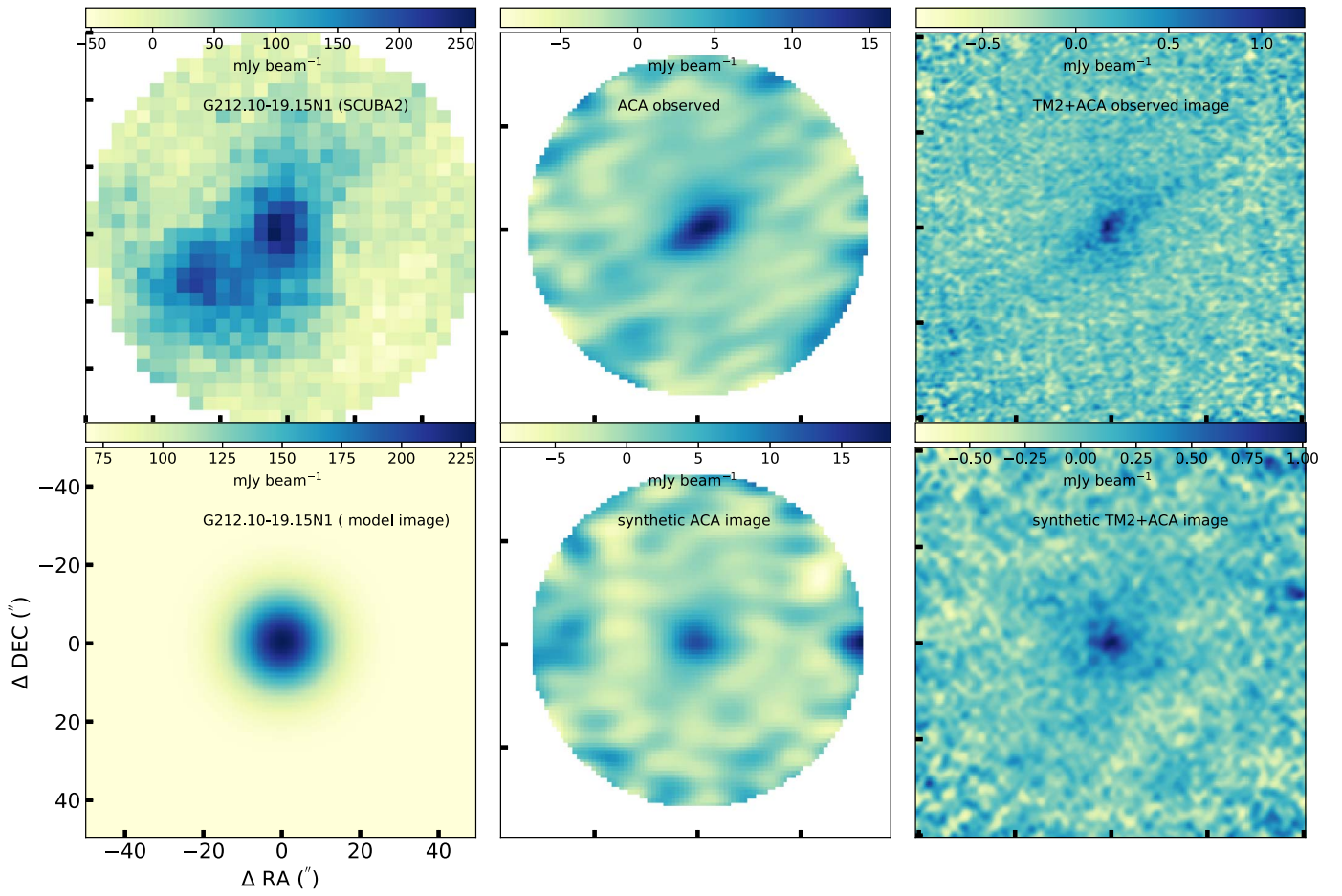


Figure B3. Top panels show the observed dust continuum from SCUBA-2, ACA, and TM2, respectively, toward the G212N1 core. The corresponding modeled synthetic images are shown in the bottom panels. The model images are based on the best-fit results that are presented in Figure 6 and Table 1.

Appendix C $\Delta\chi^2$ and Uncertainty Estimation

In this appendix, Figures C1, C2, and C3 shows $\Delta\chi^2$ plot obtained from the parameter space and used to fit the multiscale observations, respectively, for G205M3, G209N, and G212N1.

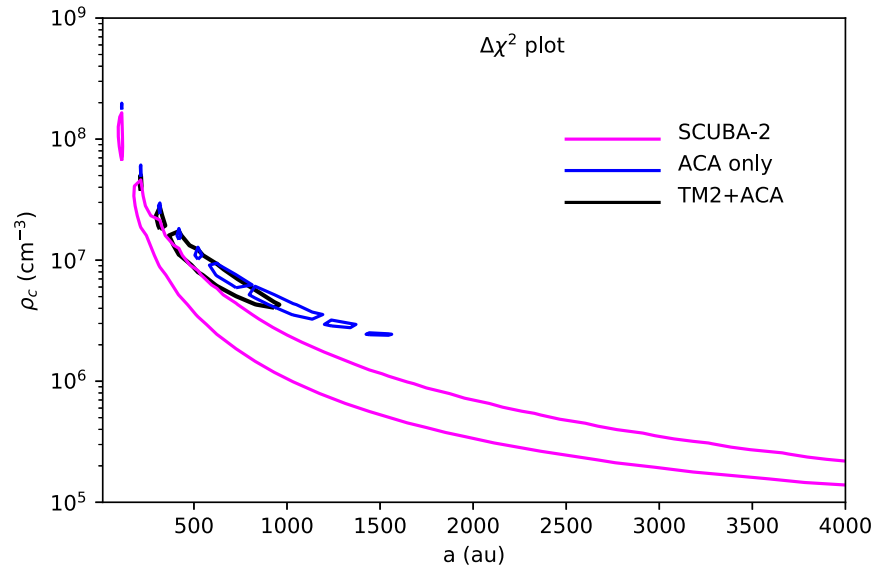


Figure C1. $\Delta\chi^2$ plot as obtained from the parameter space used to fit the multiscale observations from SCUBA-2 to ALMA for the G205M3 core.

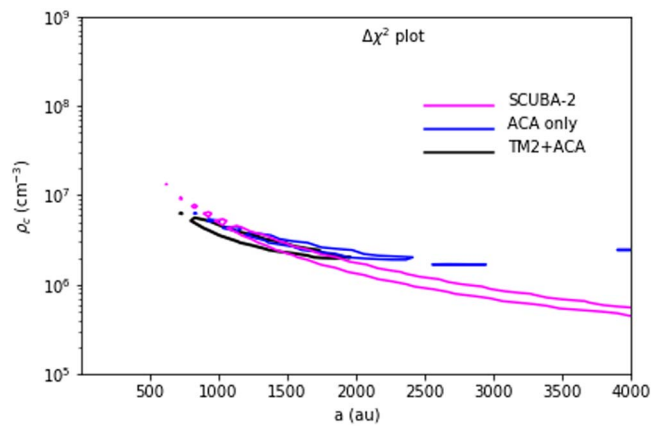


Figure C2. $\Delta\chi^2$ plot for the G209N core, similar to Figure 12.

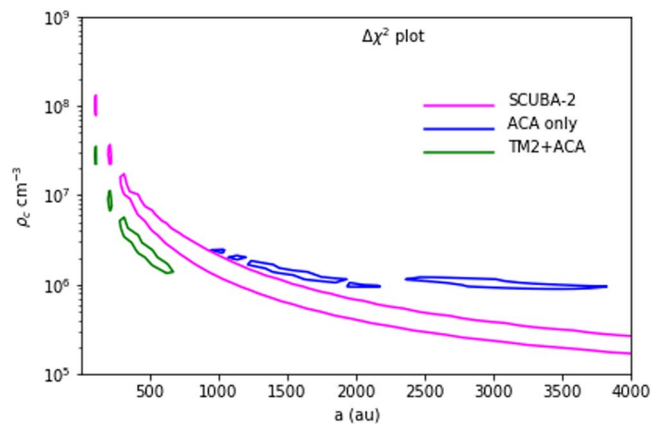


Figure C3. $\Delta\chi^2$ plot for the G212N1 core, similar to Figure 12.

ORCID iDs

Dipen Sahu  <https://orcid.org/0000-0002-4393-3463>
 Sheng-Yuan Liu  <https://orcid.org/0000-0003-4603-7119>
 Doug Johnstone  <https://orcid.org/0000-0002-6773-459X>
 Tie Liu  <https://orcid.org/0000-0002-5286-2564>
 Neal J. Evans II  <https://orcid.org/0000-0001-5175-1777>
 Naomi Hirano  <https://orcid.org/0000-0001-9304-7884>
 Ken'ichi Tatematsu  <https://orcid.org/0000-0002-8149-8546>
 James Di Francesco  <https://orcid.org/0000-0002-9289-2450>
 Chin-Fei Lee  <https://orcid.org/0000-0002-3024-5864>
 Kee-Tae Kim  <https://orcid.org/0000-0003-2412-7092>
 Somnath Dutta  <https://orcid.org/0000-0002-2338-4583>
 Shih-Ying Hsu  <https://orcid.org/0000-0002-1369-1563>
 Shanghuo Li  <https://orcid.org/0000-0003-1275-5251>
 Qiu-Yi Luo  <https://orcid.org/0000-0003-4506-3171>
 Patricio Sanhueza  <https://orcid.org/0000-0002-7125-7685>
 Hsien Shang  <https://orcid.org/0000-0001-8385-9838>
 Alessio Traficante  <https://orcid.org/0000-0003-1665-6402>
 Mika Juvela  <https://orcid.org/0000-0002-5809-4834>
 Chang Won Lee  <https://orcid.org/0000-0002-3179-6334>
 David J. Eden  <https://orcid.org/0000-0002-5881-3229>
 Paul F. Goldsmith  <https://orcid.org/0000-0002-6622-8396>
 Leonardo Bronfman  <https://orcid.org/0000-0002-9574-8454>
 Woojin Kwon  <https://orcid.org/0000-0003-4022-4132>
 Jeong-Eun Lee  <https://orcid.org/0000-0003-3119-2087>
 Yi-Jehng Kuan  <https://orcid.org/0000-0002-4336-0730>

References

- Alves, J. F., Lada, C. J., & Lada, E. A. 2001, *Natur*, 409, 159
 Andre, P., Ward-Thompson, D., & Barsony, M. 2000, in *Protostars and Planets IV*, ed. V. Mannings, A. P. Boss, & S. S. Russell (Tucson, AZ: Univ. Arizona Press), 59
 Andre, P., Ward-Thompson, D., & Motte, F. 1996, *A&A*, 314, 625
 Bacmann, A., André, P., Puget, J. L., et al. 2000, *A&A*, 361, 555
 Bonnar, W. B. 1956, *MNRAS*, 116, 351
 Caselli, P., Pineda, J. E., Zhao, B., et al. 2019, *ApJ*, 874, 89
 Caselli, P., Walmsley, C. M., Zucconi, A., et al. 2002, *ApJ*, 565, 331
 Chacon-Tanarro, A., Pineda, J. E., Caselli, P., et al. 2019, *A&A*, 623, A118
 Ciolek, G. E., & Basu, S. 2000, *ApJ*, 529, 925
 Crapsi, A., Caselli, P., Walmsley, C. M., et al. 2004, *A&A*, 420, 957
 Crapsi, A., Caselli, P., Walmsley, C. M., et al. 2005, *ApJ*, 619, 379
 Crapsi, A., Caselli, P., Walmsley, M. C., & Tafalla, M. 2007, *A&A*, 470, 221
 Dapp, W. B., & Basu, S. 2009, *MNRAS*, 395, 1092
 di Francesco, J., Evans, N. J. I., Caselli, P., et al. 2007, in *Protostars and Planets V*, ed. B. Reipurth, D. Jewitt, & K. Keil (Tucson, AZ: Univ. Arizona Press), 17
 Dutta, S., Lee, C.-F., Liu, T., et al. 2020, *ApJS*, 251, 20
 Ebert, R. 1955, *ZAp*, 37, 217
 Gomez, G. C., Vazquez-Semadeni, E., & Palau, A. 2021, *MNRAS*, 502, 4963
 Holland, W. S., Bintley, D., Chapin, E. L., et al. 2013, *MNRAS*, 430, 2513
 Hung, C.-L., Lai, S.-P., & Yan, C.-H. 2010, *ApJ*, 710, 207
 Juvela, M., Ristorcelli, I., Marshall, D. J., et al. 2015, *A&A*, 584, A93
 Keto, E., & Caselli, P. 2008, *ApJ*, 683, 238
 Keto, E., & Caselli, P. 2010, *MNRAS*, 402, 1625
 Keto, E., Rawlings, J., & Caselli, P. 2014, *MNRAS*, 440, 2616
 Kwon, W., Looney, L. W., Mundy, L. G., Chiang, H.-F., & Kemball, A. J. 2009, *ApJ*, 696, 841
 Larson, R. B. 1969, *MNRAS*, 145, 271
 McMullin, J. P., Waters, B., Schiebel, D., Young, W., & Golap, K. 2007, in *ASP Conf. Ser. 376, Astronomical Data Analysis Software and Systems XVI*, ed. R. A. Shaw, F. Hill, & D. J. Bell (San Francisco, CA: ASP), 127
 Ohashi, N., Lee, S. W., Wilner, D. J., & Hayashi, M. 1999, *ApJL*, 518, L41
 Ohashi, S., Sanhueza, P., Sakai, N., et al. 2018, *ApJ*, 856, 147
 Ossenkopf, V., & Henning, T. 1994, *A&A*, 291, 943
 Sadavoy, S. I., Stutz, A. M., Schnee, S., et al. 2016, *A&A*, 588, A30
 Sahu, D., Liu, S.-Y., Liu, T., et al. 2021, *ApJL*, 907, L15
 Schmalzl, M., Launhardt, R., Stutz, A. M., et al. 2014, *A&A*, 569, A7
 Shirley, Y. L., Evans, N. J. I., Rawlings, J. M. C., & Gregersen, E. M. 2000, *ApJS*, 131, 249
 Shu, F. H. 1977, *ApJ*, 214, 488
 Tafalla, M., Myers, P. C., Caselli, P., & Walmsley, C. M. 2004, *A&A*, 416, 191
 Tafalla, M., Myers, P. C., Caselli, P., Walmsley, C. M., & Comito, C. 2002, *ApJ*, 569, 815
 Ward-Thompson, D., Motte, F., & Andre, P. 1999, *MNRAS*, 305, 143
 Ward-Thompson, D., Scott, P. F., Hills, R. E., & Andre, P. 1994, *MNRAS*, 268, 276
 Whitworth, A. P., & Ward-Thompson, D. 2001, *ApJ*, 547, 317
 Yi, H.-W., Lee, J.-E., Liu, T., et al. 2018, *ApJS*, 236, 51